Quantitatively Accurate Image Reconstruction for Clinical Whole-Body PET Imaging

Evren Asma*, Sangtae Ahn*, Hua Qian*, Girishankar Gopalakrishnan†,
Kris Thielemans‡, Steven G. Ross§, Ravindra M. Manjeshwar* and Alexander Ganin§
* General Electric Global Research Center, Niskayuna, NY, 12309
E-mail: {asma,ahns,qianh,manjeshw}@research.ge.com
† GE Healthcare, Bangalore, India
E-mail:girish.gopalakrishnan@ge.com
‡ King's College School of Medicine, London, UK
E-mail: kris.thielemans@kcl.ac.uk
§ General Electric Healthcare, Milwaukee, WI, 53188
E-mail: {steven.ross,alexander.ganin}@med.ge.com

***Abstract*—We present a PET image reconstruction approach that aims for accurate quantitation through model-based physical corrections and rigorous noise control with clinically acceptable image properties. We focus particularly on image generation chain components that are critical to quantitation such as physical system modeling, scatter correction, patient motion correction and regularized image reconstruction. Through realistic clinical datasets with inserted lesions, we demonstrate the quantitation improvements due to detector point spread function modeling, model-based single scatter estimation and the associated object-dependent multiple scatter estimation and non-rigid patient motion estimation and motion correction. We also describe a penalized-likelihood (PL) whole-body clinical PET image reconstruction approach using the relative difference penalty that achieves superior quantitation over the clinically-widespread ordered subsets expectation maximization (OSEM) algorithm while maintaining visual image properties similar to OSEM and therefore clinical acceptability. We discuss the axial and in-plane smoothing modulation profiles that are necessary to avoid large variations in noise and resolution levels. The overall approach of accurate models for data acquisition, corrections for patient related effects and rigorous noise control greatly improve quantitation and when combined with repeatable imaging protocols, limit quantitation variability only to factors related to patient physiology and scanner performance differences.**

I. Introduction

As Positron Emission Tomography (PET) is more commonly used for diagnosis, staging, and therapy response evaluation, accurate quantitation becomes increasingly important for prognosis and response monitoring [1]. PET quantitation however, is affected by many factors such as injection and scan protocols [2], [3], patient biology [4], scanner properties and image reconstruction methods and parameters [3].

The PET data acquisition process includes scanner and patient dependent physical effects that can affect quantitation if they are not correctly accounted for during the reconstruction. Patient related effects include scatter [10], [11], [12], attenuation and voluntary and involuntary motion [24], [25] while scanner related effects include blurring at the detectors due to crystal penetration and inter-crystal scatter [5], [14], [15] as well as variations in detector sensitivities.

Patient motion during a PET/CT scan that typically lasts several minutes per bed position can result in compromised lesion detection and quantitation. Correcting for patient motion also requires matched PET and CT images. In addition to these physical effects PET imaging suffers from a limited number of detected photons that requires some form of explicit or implicit noise control [6]. Current clinical practice uses the ordered subsets expectation maximization (OSEM) algorithm that controls noise through underconvergence and post-filtering which affects quantitation.

In this paper we describe accurate, model-based corrections for physical effects and demonstrate how quantitation can be improved by accurate models, corrections and explicit noise control through regularization while avoiding image artifacts such as blocky organs or patchy noise textures.

II. Background

A. Forward Model

We use the following factored forward model for PET data generation that relates the mean measured data $\bar{\mathbf{y}}$ to the activity distribution $\mathbf{x}$ that is being estimated [5]:

$$\bar{\mathbf{y}} = \mathbf{P}_{norm}\mathbf{P}_{psf}\mathbf{P}_{attn}\mathbf{P}_{geom}\mathbf{x} + \hat{\mathbf{s}} + \hat{\mathbf{r}} \quad (1)$$

where the ij^{th} element of the system matrix $\mathbf{P} \equiv \mathbf{P}_{norm}\mathbf{P}_{psf}\mathbf{P}_{attn}\mathbf{P}_{geom}$ contains the probability of an annihilation at voxel j being detected at detector pair i and is composed of normalization, detector point-spread-function, attenuation and geometric components. Additive background terms $\hat{\mathbf{s}}$ and $\hat{\mathbf{r}}$ are

mean scatter and random coincidences that are estimated prior to the reconstruction.

For a motion-gated dataset with mean data $\bar{\mathbf{y}}_g$ at gate g and known or estimated patient motion, the forward model becomes [25]:

$$\bar{\mathbf{y}}_g = \mathbf{P}_{norm}\mathbf{P}_{psf}\mathbf{P}_{attn}\mathbf{P}_{geom}\mathbf{W}_g\mathbf{x} + \hat{\mathbf{s}} + \hat{\mathbf{r}} \quad (2)$$

where $\mathbf{W}_g$ is the warping matrix that relates the reference activity distribution $\mathbf{x}$ to the activity distribution in gate g due to motion: $\mathbf{W}_g\mathbf{x}$.

B. Forward Model Formation

The geometric detection probability matrix $\mathbf{P}_{geom}$ is efficiently calculated on-the-fly using "distance-driven" projectors [7], [8] that are based on computing the overlap between detector boundaries and image voxel boundaries on a common plane. $\mathbf{P}_{attn}$ is a diagonal matrix of attenuation correction factors whose elements are formed by converting the patient's CT image into attenuation maps at 511 keV [16] and applying Beer's law - i.e. $\exp(-\int_L \mu d\ell)$. The elements of $\mathbf{P}_{norm}$ account for sensitivity variations due to geometry and detector efficiencies. These calibration factors are measured using a combination of rotating sources (line, plane, flood etc.). $\mathbf{P}_{psf}$ is measured by placing point sources at various locations within the field-of-view.

Mean scatter events ($\mathbf{s}$) are estimated by first forming a model-based mean single-scatter sinogram estimate [10], followed by multiple-scatter estimation by filtering the single-scatter estimate and finally performing tail-scaling to ensure that the overall scatter estimate is correctly scaled. Mean random coincidences $\mathbf{r}$ are estimated either from a smoothed version of the delayed events [17] or from the singles rates [18].

Our focus is on the quantitation effects of the following components each of which can have significant effects on both quantitation and visual image quality:

- Detector point spread function (PSF) estimation and modeling that forms $\mathbf{P}_{psf}$
- Model-based mean scatter activity estimation and correction ($\hat{\mathbf{s}}$)
- Motion estimation to form the warping matrix W_g and motion corrected image reconstruction
- Convergent reconstruction of $\mathbf{x}$ from measured data $\mathbf{y}$ under the forward model (1) with rigorous noise control

C. Penalized Likelihood Image Reconstruction

Image reconstruction is performed by maximizing the following penalized-likelihood objective function over all non-negative images, assuming a Poisson model for the data:

$$\Phi(\mathbf{x}) = \sum_{i=1}^{n_d} y_i log\bar{y}_i - \bar{y}_i - \beta \sum_{j=1}^{n_v} \sum_{k\in\mathcal{N}_j} w_j w_k \phi(x_j - x_k) \quad (3)$$

where n_d and n_v denote the number of detectors and voxels respectively, $\bar{y}_i \equiv [P\mathbf{x}]_i + \hat{r}_i + \hat{s}_i$, β is the global smoothing parameter controlling overall penalty strength, w_j and w_k are penalty weights modulating the local penalty strength and $\phi(\cdot)$ is a potential function penalizing the difference between neighboring voxels. Quantitation and subjective image properties such as organ uniformity, organ boundary sharpness, background noise texture depend heavily on the particular penalty $\phi(\cdot)$ and local penalty strength as determined by β and its modulation.

There are several globally convergent numerical optimization algorithms that are designed to optimize this cost function for convex penalties with bounded second derivatives such as BSREM [19], [21], COSEM [20] and OSEM-MAP [22]. We chose BSREM due to its convergence speed away from the solution, automatic incorporation of the positivity constraint and ease of applicability to different penalties.

III. Methods for Quantitative Imaging

A. Quantitation Evaluation with Hybrid Datasets

In order to perform quantitation analysis with clinical datasets and known ground truth, we inserted lesions of known size and activity into patient datasets. This was accomplished by generating high resolution lesions, forward projecting them with the entire system model accounting for geometry, patient-specific attenuation, detector blurring and detector normalization and finally adding the resulting projections to the original dataset. Scatter and random sinograms were assumed to be unaffected by the lesions that occupy a very small fraction of the activity distribution.

Lesions were inserted in various locations where algorithmic properties might be different such as the liver (hot background), lung (cold background), near-liver (cold background close to hot object) and spine (center of the FOV). This "hybrid" dataset approach allows us to combine realistic clinical backgrounds (important for clinical acceptability) with known lesion activity levels (necessary for quantitative evaluations). Such a combination is neither possible with anthropomorphic phantoms due to their piecewise constant nature nor with the original clinical datasets where ground truth is not known.

The contrast metric is the ratio of mean reconstructed activity throughout the lesion region-of-interest (ROI) to the true inserted activity.

The noise metric is the ratio of the standard deviation of reconstructed activity within a large, uniform region (e.g. liver) to the mean of that activity. Such a single-image noise metric is necessary because it is not possible to generate multiple noise realizations as in the case of phantom simulations and they are good surrogates for ensemble noise metrics when the noise correlation lengths are not too long relative to ROI sizes.

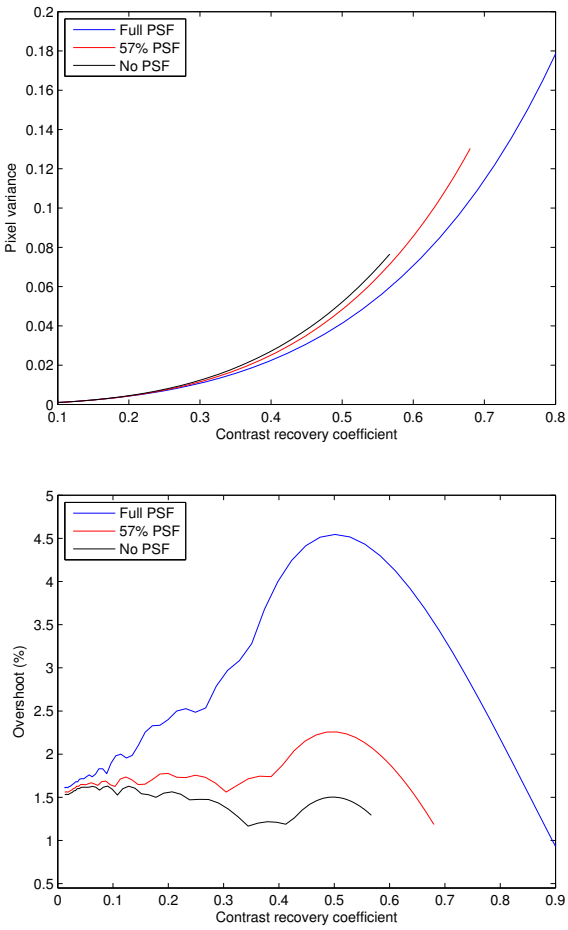

Fig. 1. Theoretical contrast versus noise (top) and contrast versus overshoot plots for different levels of detector PSF modeling for quadratically penalized PL reconstructions. Individual curves are parameterized by the smoothing parameter β.

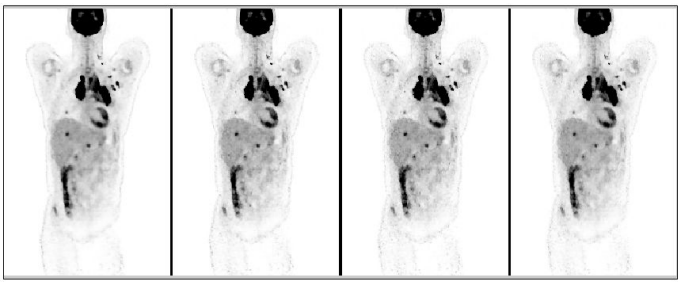

Fig. 2. Penalized likelihood images reconstructed with full, 70%, 50% and no PSF (left to right) modeling for clinical dataset anon4039. Despite the resolution and contrast loss in reconstructions with partial PSF models, there is no significant overshoot/undershoot reduction. Data courtesy of Mayo Clinic, Rochester, MN.

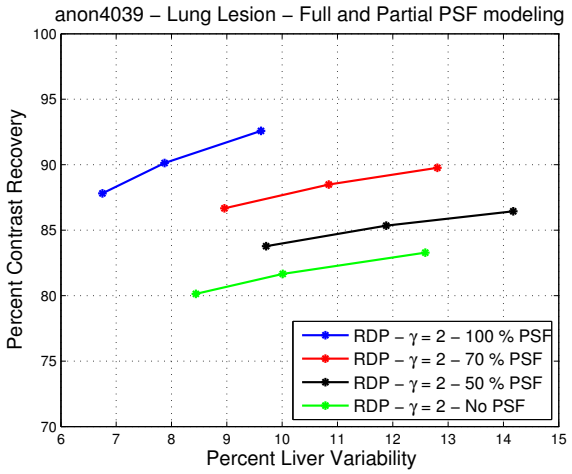

Fig. 3. Representative contrast versus liver variability curves for the inserted lung lesion in anon4039. Full PSF modeling produces the highest contrast levels at matched noise levels.

B. PSF Estimation and Modeling

Blurring of sinograms caused by physical effects such as inter-crystal scatter, detector penetration and photon pair non-collinearity are typically modeled as point spread functions (PSFs) in sinogram space and incorporated into image reconstruction (e.g., [5], [14], [15]). It is also possible to model the effect mathematically in image space [23].

While the inclusion of such detector PSF models expectedly leads to improved contrast recovery and noise, they can also produce edge artifacts, even with exact PSF modeling, which have been described as ringing and overshoot/undershoot artifacts (e.g., [5], [14], [15]). These artifacts have an impact on clinical acceptability and can be reduced by modeling the detector blurring as a narrower than actual blur; however such undermodeling comes at the cost of lower contrast and/or increased noise. As a result, there is a tradeoff between contrast, noise and ringing artifacts that are parameterized by the extent of detector modeling [9]. For the case of penalized likelihood image reconstruction with quadratic penalties, these tradeoffs can be theoretically analyzed and predicted [9]. Figure 1 shows such theoretically predicted tradeoffs between contrast, noise and ringing as a function of percent PSF modeling.

The operating point among these tradeoffs depends on the noise level in the dataset. When high count, low noise datasets are reconstructed with small voxels (e.g. brain imaging), the tradeoff primarily becomes one between contrast and ringing. In that case undermodeling the detector PSF can be a viable option for controlling ringing. On the other hand, when low count datasets are reconstructed with larger voxels, as in whole-body clinical datasets, ringing artifacts are small due to higher smoothing levels and fall below the image noise levels. Therefore the main tradeoffs are between contrast and noise.

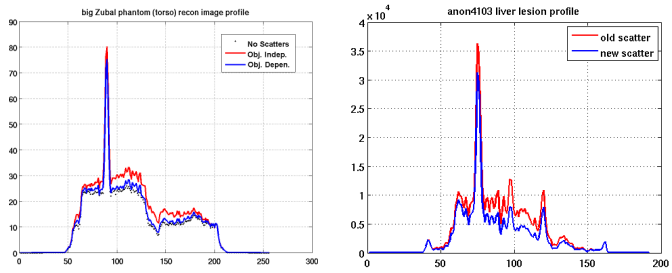

Fig. 4. Profiles from reconstructed phantom and hybrid clinical dataset images with object independent and object dependent multiple scatter estimation. Object dependent multiple scatter estimation results in approximately 10% improvement in contrast to liver variability ratios for both simulated and clinical datasets. Clinical dataset courtesy of Mayo Clinic, Rochester, MN.

Figure 2 shows reconstructions with full and partial PSF modeling and Figure 3 shows the associated contrast/noise tradeoff curves. Inclusion of full PSF models improve both contrast and noise metrics. Note that part of the single-image noise degradation in undermodeled PSF images is due to reduced correlation between voxels. The most visible visual effect of PSF modeling is sharper patient boundaries.

C. Model-Based Scatter Estimation

In 3-D PET systems scattered events can comprise approximately 40% of the total counts [10] and accurate scatter correction is therefore critical for quantitation. Most scatter estimators are model-based single scatter estimators that rely on single-scatter physics models [10], [11]. Since scatter estimation requires knowledge of the activity distribution and vice versa, scatter estimation algorithms are performed iteratively where the activity and scatter estimates are refined at each iteration. Other scatter components that present challenges for modeling are multiple scatters and scatter from outside the field-of-view [29].

Multiple scatter estimates could either be model-based at very high computational cost [27] or in the form of smoothed versions of the single-scatter sinogram (SSS) estimate [28]. Even though multiple scatters form only approximately 15% of total scattered events [13], it plays an important role in determining the overall scatter contribution. Scatter contributions that come from outside the scanned field of view can be estimated by accounting for one bed position on either side of the reconstructed bed position in the model-based single scatter estimator which results in additional computational cost [29].

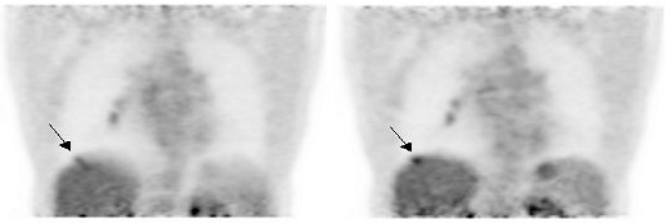

Fig. 5. Gate-averaged images before (left) and after motion correction illustrating reduced motion blur and improvement in tumor conspicuity. For this case the SUVmax increased from 9.5 kBq/ml to 11.94 kBq/ml whereas the volume reduced from 6.35 ml to 4.04 ml. Dataset courtesy of Cancer Treatment Centers of America, Tulsa, OK.

We had previously implemented and evaluated a fully 3D scatter sinogram estimation algorithm [12] based on the single-scatter estimation model in [10]. Shift-invariant SSS smoothing is not robust across object sizes because the extent of multiple scatters depend on the object. For this reason we performed an object-dependent smoothing of the SSS where the smoothing kernel parameters, amplitude and width, at each sinogram point depend linearly on the total object path length seen by the line-of-response [30]. These path lengths are obtained from the CT image of the patient that is readily available in clinical PET/CT systems. The form of the object dependent smoothing and their dependences on path lengths are as follows:

$$k(u;r,\phi) = \frac{A(r,\phi)}{\sigma(r,\phi)} exp\left(-\frac{-u^2}{2\sigma^2(r,\phi)}\right) \quad (4)$$

$$A(r,\phi) = a \cdot \ell_f(r,\phi) + b \quad (5)$$

$$\sigma(r,\phi) = c \cdot \ell_f(r,\phi) + d \quad (6)$$

where $\ell_f(r,\phi)$ denotes the path length along the line of response, $A(r,\phi)$ and $\sigma(r,\phi)$ are the object dependent kernel amplitude and with respectively. The linear model parameters (a,b,c,d) were determined for a given scanner geometry and detector energy resolution by performing least square fits over a range of object sizes.

Figure 4 shows reconstructed image profiles across inserted lesions that estimated multiple scatters from object dependent and independent smoothing of the SSS. Improved multiple scatter estimation improves quantitation by approximately 10% for both the simulated and hybrid clinical datasets.

D. Motion Corrected Image Reconstruction

Patient motion such as respiratory motion is an important factor affecting PET quantitation in regions affected by the motion. Respiratory motion can cause lesions motion of up to several centimeters and therefore result in the overestimation of the lesion size and underestimation of lesion contrast [34], [35].

Motion correction approaches consist of three stages: (i) data binning, (ii) motion vector estimation (iii) motion corrected image reconstruction.

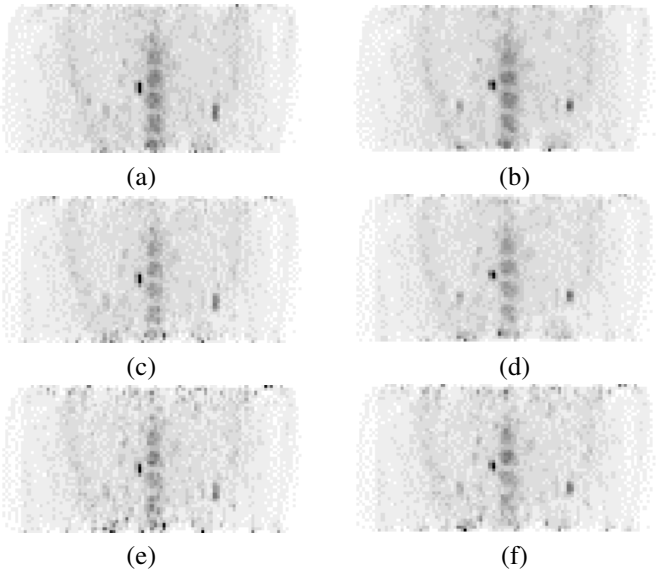

Fig. 6. Images showing the improvement after motion correction (right) for high count (a)-(b), medium count (c)-(d) and (e)-(f) low count cases which correspond to 250 , 125 and 80 seconds of acquisition time respectively. Data courtesy of Hospitale San Raffaele, Milan.

Although there is no established "best" data binning scheme, a common approach to binning is based on the displacement of an external motion tracker where data collected within each predefined displacement range is assigned to the same bin (displacement binning e.g. [31]). Some of the other binning approaches include phase binning that is based on the patient's phase within a respiratory/cardiac cycle (e.g. [33]) and quiescent period binning [32] that only uses data from the breathing cycle during which there is minimal motion.

Motion vector estimation is performed by registering gated CT or gated PET images to a reference gate. Registration of PET images instead of CT images avoids any PET-CT gate mismatch problems since PET and CT are acquired sequentially. We applied a multiresolution version of the level-sets algorithm [36] on gated PET images to [37] to obtain the motion vectors. The displacement field is updated according to:

$$\mathbf{v}_{n+1}(\mathbf{x}) = \mathbf{v}_n(\mathbf{x}) + [\mathbf{I}_R - \mathbf{I}_g(\mathbf{v}(\mathbf{x}))]\frac{\nabla \mathbf{I}_g(\mathbf{v}(\mathbf{x}))}{||\nabla \mathbf{I}_g(\mathbf{v}(\mathbf{x}))||} \tag{7}$$

where $\mathbf{I}_R$ is the reference image and $\mathbf{I}_g$ is the registered image and $\mathbf{v}(\mathbf{x})$ denotes the displacement vector at $\mathbf{x}$ and $\mathbf{v}$ is initialized with zero displacement.

Motion corrected image reconstruction techniques fall under two main categories: (i) Each gated image is reconstructed independently, registered to a reference gate and the results are averaged (possibly with weights) to form the final motion corrected image (e.g. [24], [25]). We call this method RRA (Reconstruct, Register and Average) (ii) Motion information is included in the large system model that accounts for all gates and the single, motion corrected image is directly reconstructed (e.g. [26], [38]). We call this method MBMC (Model-Based Motion Correction). The modeling equations for RRA and MBMC are as follows:

RRA:

$$\bar{\mathbf{y}}_g = \mathbf{P}\mathbf{x}_g \quad g = 1, \ldots, G$$

$$\hat{\mathbf{x}}_g = \arg\max_{\mathbf{x}\geq \mathbf{0}} L(\mathbf{y}_g|\mathbf{x};\mathbf{P}) - \beta \mathbf{R}(\mathbf{x})$$

$$\hat{\mathbf{x}}_{RRA} = \frac{1}{G}\sum_{g=1}^{G} \mathbf{W}_g^{-1}\hat{\mathbf{x}}_g \tag{8}$$

MBMC:

$$\bar{\mathbf{y}} \equiv \begin{bmatrix} \bar{\mathbf{y}}_1 \\ \vdots \\ \bar{\mathbf{y}}_G \end{bmatrix} = \begin{bmatrix} \mathbf{P}\mathbf{W}_1 \\ \vdots \\ \mathbf{P}\mathbf{W}_G \end{bmatrix} \mathbf{x} \equiv \mathbf{P}_{BIG}\mathbf{x}$$

$$\hat{\mathbf{x}}_{MBMC} = \arg\max_{\mathbf{x}\geq \mathbf{0}} L(\mathbf{y}|\mathbf{x};\mathbf{P}_{BIG}) - \beta \mathbf{R}(\mathbf{x}) \tag{9}$$

where G is the total number of gates, $L(\mathbf{y}|\mathbf{x};\mathbf{P}) = \sum_{i=1}^{n_d} y_i \log(\mathbf{P}\mathbf{x})_i - (\mathbf{P}\mathbf{x})_i$ denotes the Poisson log-likelihood with data $\mathbf{y}$, candidate image $\mathbf{x}$ and system matrix $\mathbf{P}$ and $\mathbf{W}_g$ denotes the warping matrix that relates true activity at gate g to true activity at the reference gate. Both of these techniques require matched gated CT images for attenuation correction which can be acquired within acceptable dose levels by using low-dose CT data acquisition and image reconstruction techniques [47], [48].

While MBMC has been shown to be quantitatively more accurate [26], [38] due to its ability to account for variations in detection probabilities between gates, RRA has the practical advantage of post gated-reconstruction applicability and quantitation performance comparable to MBMC at medium and high levels of smoothing [26], especially when gates are of similar duration [38].

Figure 5 shows a clinical case in which a tumor in the liver that was indistinct in the ungated imaged becomes significantly more prominent after respiratory motion correction. The correction brought about a 36.3% decrease in volume, a 25.7% increase in the SUVmax.

Figure 6 shows results from a clinical case (top row) as well as its lower count scan versions where data from only half and one-third of the scan are used. For the lesion to the right of the spine in the image (left in patient), lesion motion is approximately 12 mm and average SUVmax increase across all count levels is 20%. For the smaller lesion immediately left of the spine, lesion motion is approximately 7 mm and average SUVmax is reduced by 17% due to interpolations in the motion estimates. This case illustrates difficulties that may occur with respiratory

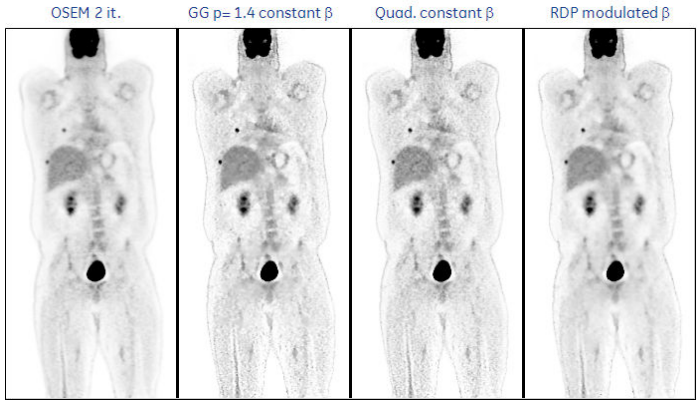

Fig. 7. Images reconstructed (from left to right) with OSEM (2 it.), generalized Gaussian penalty p=1.4 ($\beta = 325$), quadratic penalty ($\beta = 15000$) and RDP ($\beta = 325$) for anon4127. Bed overlap regions are oversmoothed and noise in cold regions is blocky in the generalized Gaussian and quadratic penalty reconstructions with constant smoothing parameters. Datasets courtesy of Mayo Clinic, Rochester, MN.

motion correction when the extent of motion is small compared to lesion size and/or when lesions are small compared to voxel size. It is also notable that the tumor motion is accurately recovered in both the half and one-third count cases.

E. Quantitative PL Image Reconstruction with Clinically Acceptable Images

Despite the fact that penalized likelihood image reconstruction methods have been published and analyzed since the late 80s, (e.g. [39], [41]) their clinical applicability has been hindered by increased computational cost and tradeoffs between quantitation and visual image quality (e.g. blocky organs, patchy organ and background noise textures etc.). The commonly used penalties were the quadratic penalty ($\phi(r) = r^2$) that produced natural looking images but with limited quantitation improvements or edge-preserving penalties such as generalized Gaussian ($\phi(r) = r^p$), log-cosh or Huber [40] with greater improvements in quantitation but unnatural looking, blocky images.

Another important factor affecting both image quality and quantitation is smoothing modulation. When a constant smoothing parameter is used, low sensitivity regions within the field-of-view (FOV) such as axial planes towards the edge of the FOV are oversmoothed, causing blurry bed-overlap regions. This effect is related to the uniform variance properties of the quadratic penalty [45].

Although modulated quadratic penalty weights were derived for target resolution properties such as uniform resolution [46] and isotropic resolution [42], such properties can come at the expense of undesirably large noise strength variations throughout the FOV. The second and third images in Figure 7 show reconstructions using constant smoothing parameters where the blurry overlap regions (due to oversmoothing) and patchy background

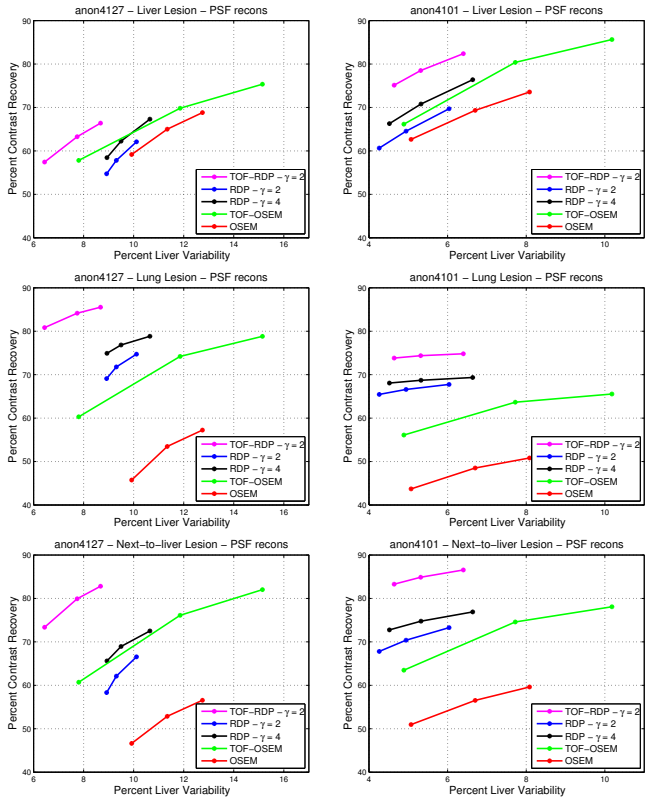

Fig. 8. Contrast vs. liver variability curves for clinical dataset anon4127 (left) and anon4101 (right) for three of the five inserted lesions at the liver, lung and near-liver (top to bottom) for time-of-flight (TOF) and non-TOF reconstructions . RDP and OSEM curves are parameterized by β and iteration number, respectively. Quantitation improvements with RDP and spatially modulated smoothing are comparable to quantitation differences between TOF-OSEM and non-TOF OSEM. Datasets courtesy of Mayo Clinic, Rochester, MN.

noise textures (due to approximately uniform noise in hot organs and cold background) are visible.

In order to treat noise differently in hot organs and cold background regions, Nuyts et al proposed the following convex, relative difference penalty (RDP) [43] and demonstrated improved lesion detection performance compared to the standard quadratic penalty [44]:

$$R(\mathbf{x}) = \sum_{j=1}^{n_v} \sum_{k \in \mathcal{N}_j} \frac{w_j w_k (x_j - x_k)^2}{x_j + x_k + \gamma |x_j - x_k|} \tag{10}$$

Note that depending on the choice of edge-preservation level parameter γ, the RDP penalty behaves as a combination of a quadratic penalty with activity dependent smoothing and an edge-preserving generalized Gaussian penalty. The activity dependent smoothing property of RDP ensures that regions of low activity are smoothed heavier and vice versa. This property is very similar to that of commonly used, early-stopped OSEM where low activity regions are smoother due to slower convergence. As a

result, RDP produces images with visual noise properties similar to that of OSEM while maintaining quantitation advantages due to full convergence and more rigorous noise control. These similarities can be seen by comparing the first and fourth images in Figure 7.

The γ parameter is chosen based on the tradeoff between quantitation accuracy and clinical acceptability. Higher γ values provide more accurate quantitation due to improved edge-preservation; however very large γ values result in blocky, clinically unacceptable images. Therefore the preferred γ is the largest possible value that avoids blockiness and maintains clinical acceptability.

In order to avoid oversmoothing in bed-overlap regions, we performed modulated smoothing with separate axial and transaxial modulation components. The axial profile followed the sensitivity profile except for flat bed-overlap regions (i.e. sensitivity profile accounting for the next bed-position). Transaxially, smoothing increased linearly with distance away from the center. These data-independent profiles mimic the uniform resolution kernels in [46] but vary slower throughout the FOV therefore avoiding both oversmoothing and undersmoothing of low sensitivity regions that may occur when noise and resolution uniformity are targeted respectively. Overall, these smoothing profiles provide a reasonable, computationally efficient and object-independent trade-off between noise and resolution uniformity.

Representative reconstructed images are shown in Figure 7 and contrast versus liver-variability trade-off curves for two clinical datasets are shown in Figure 8. Liver variability serves as the single-image noise metric in these hybrid datasets. We see that the RDP penalty images have superior quantitation in all five lesions for both clinical datasets. Largest quantitation improvements occur for the lung and near-liver lesions due to OSEM's slow convergence in cold regions and near hot objects, respectively.

Figure 9 shows contrast values at matched noise levels for lesion contrasts of 1.5, 2, 3, 4 and 8 to 1. Together, these curves demonstrate the robustness of the improved quantitation across count levels and lesion contrast levels. The results shown here are for non time-of-flight (TOF) PET imaging and their application to TOF imaging would further improves quantitation.

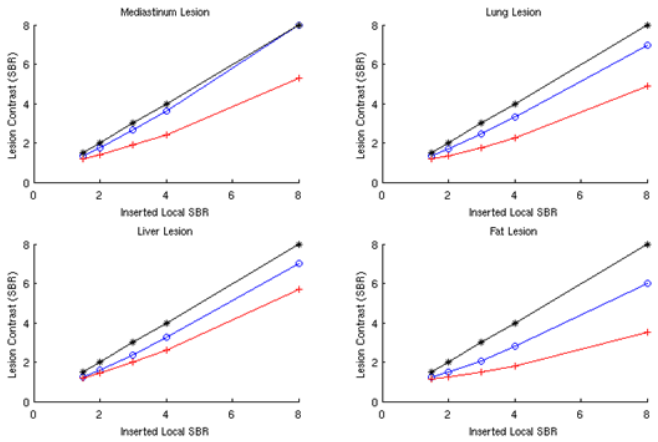

Fig. 9. Reconstructed vs. true contrast curves for lung, liver, mediastinum and fat lesions at approximately matched liver variability (noise metric) levels for anon4039. Black curves correspond to ideal reconstructions where recovered contrast exactly equals true contrast, blue curves are for PL reconstructions with RDP and red curves are for OSEM. All reconstructions include full PSF modeling.

IV. Conclusions and Discussion

We have presented corrections for the components of the PET data acquisition and image reconstruction chain that are critical to quantitation and showed how quantitation can be improved through these corrections. We also showed that when these corrections are used in conjunction with regularized image reconstruction techniques that explicitly and predictably control noise, quantitation can be further improved over algorithms that implicitly control noise through early stopping.

The resulting image reconstruction approach considers all aspects of the imaging chain and the cumulative effect of all improvements, small and large, makes PET an even more reliable and accurate tool for quantitation, thereby improving its applications such as cancer staging, deciding on whether or not a patient responds to therapy, the extent of the response and the prognosis.

References

[1] R. Boellaard, "Standards for PET image acquisition and quantitative data analysis", *Jour. Nuc. Med.*, 50(5):12S-20S, 2009

[2] V.J. Lowe, D.M. DeLong, J.M. Hoffman, R.E. Coleman, "Optimum scanning protocol for FDG-PET evaluation of pulmonary malignancy", *Jour. Nuc. Med.*, 36(5):883-887, 1995

[3] R. Boellaard, N.C. Krak, O.S. Hoekstra, A.A. Lammertsma, "Effects of noise, image resolution and ROI definition on the accuracy of standard uptake values: a simulation study", *Jour. Nuc. Med.*, 45(9):1519-1527, 2004

[4] L. Gorospe, S. Raman, J.Echevester, N. Avril, Y. Herrero, N.S. Herna, "Whole-body PET/CT: spectrum of physiological variants, artifacts and interpretative pitfalls in cancer patients", *Nucl. Med. Commun.*, 26(8):671-687, 2005

[5] J. Qi, R. M. Leahy, C. Hsu, T. H. Farquhar and S. R. Cherry, "Fully 3D Bayesian image reconstruction for the ECAT EXACT HR+", *IEEE Trans. Nucl. Sci.*, 45(3):1096-1103, 1998

[6] A.Alessio and P.E. Kinahan, "Improved quantitation for PET/CT image reconstruction with system modeling and anatomical priors", *Med. Phys.*, 33(11):4095-4103, 2006

[7] B. DeMan and S. Basu, "Distance-driven projection and backprojection in three dimensions", *Phys. Med. Bio*, 49(11):2463-2475, 2004

[8] R.M. Manjeshwar, S.G. Ross, M. Iatrou, T.W. Deller, C.W. Stearns, "Fully 3D PET iterative reconstruction using distance-driven projectors and native scanner geometry", *Proc. IEEE Nuc. Sci. Symp. Med. Img. Conf.* pp. 2804-2807 , 2006

[9] S. Ahn, E. Asma, K.Thielemans, T. Deller, S. Ross and C.W. Stearns, "Trade-off between contrast recovery, image noise and edge-artifacts in PET image reconstruction using detector blurring models", *Proc. IEEE Nuc. Sci. Symp. Med. Img. Conf.* pp. 4110-4114, 2011

[10] J. Ollinger, "Model-based scatter correction for fully 3D PET", *Phys. Med. Bio*, 41(1):153-176, 1996

[11] C.C. Watson, "New, faster, image-based scatter correction for 3D PET", *IEEE Trans. Nuc. Sci.*, 47(4):1587-1594, 2000

[12] M. Iatrou, S.G. Ross, R.M. Manjeshwar, C.W. Stearns, "3D implementation of scatter estimation in 3D PET", *Proc. IEEE Nuc. Sci. Symp. Med. Img. Conf.* pp. 2142-2145, 2006

[13] L.G. Hiltz and B.T.A McKee, "Scatter correction for three-dimensional PET based on an analytic model dependent on source and attenuating object", *Phys. Med. Bio*, 39(11):2059-2071, 1994

[14] V.Y. Panin, F. Kehren, M. Rothfuss, D. Hu, C. Michel, M.E. Casey, "PET reconstruction with system matrix derived from point source measurements", *IEEE Trans. Nucl. Sci.*, 53(1):152-159, 2006

[15] A.M. Alessio, C.W. Stearns, S. Tong, S.G. Ross, S. Kohlmyer, A. Ganin and P.E. Kinahan, "Application and Evaluation of a Measured Spatially Variant System Model for PET Image Reconstruction", *IEEE Trans. Med. Imag.*, 29(3):938-949, 2010

[16] P.E. Kinahan, D.W. Townsend, T. Beyer, D.Sashin, "Attenuation correction for a PET/CT scanner", *Med. Phys.*, 25(10):2046-053, 1998

[17] M.E. Casey, E.J. Hoffman, "Quantitation in positron emission computed tomography: 7. A technique to reduce noise in accidental coincidence measurements and coincidence efficiency calibration", *Jour. Comp. Assist. Tomog.*, 10(5):845-850, 1986

[18] C.W.Stearns, D.L. McDaniel, S.G. Kohlmyer, P.R. Arul, B.P. Geiser, V. Shanmugam, "Random coincidence estimation from single event rates on the Discovery ST PET/CT scanner", , *Proc. IEEE Nuc. Sci. Symp. Med. Img. Conf.*, pp. 3067-3069, 2003

[19] S. Ahn and J.A. Fessler, "Globally convergent image reconstruction for emission tomography using relaxed ordered subsets algorithms," *IEEE Trans. Med. Imag.*, 22(5):613–626, 2003

[20] I.T. Hsiao, A. Rangarajan, P.Khurd, G. Gindi, "An accelerated convergent ordered subsets algorithm for emission tomography", *Phys. Med. Bio.* 49(11):2145-2156, 2004

[21] A.R. DePierro, M.E.B. Yamagishi, "Fast EM-like methods for maximum "a-posteriori" estimates in emission tomography", *IEEE Trans. Med. Imag.*, 20(4):280-288, 2001

[22] A. R. De Pierro, "A modified expectation maximization algorithm for penalized likelihood estimation in emission tomography", *IEEE Trans. Med. Imag.*, 14(1):132-137, 1995.

[23] E. Rapisarda, V. Bettinardi, K. Thielemans and M. C. Gilardi, "Image-based point spread function implementation in a fully 3D OSEM reconstruction algorithm for PET", *Phys. Med. Bio.* 55(14):4131-4151, 2010

[24] P. Kinahan, L. MacDonald, L. Ng, A. Alessio, P. Segars, B. Tsui, "Compensating for patient respiration in PET/CT imaging with the registered and summed phases (RASP) procedure" *Proc. IEEE Int. Symp. Bio. Imag.*, pp. 1104-1107, 2006

[25] R. Manjeshwar, X. Tao, E. Asma, K. Thielemans, "Motion compensated image reconstruction of respiratory gated PET/CT", *Proc. IEEE Int. Symp. Bio. Imag.*, pp. 674-677, 2006

[26] E. Asma, R. Manjeshwar, K. Thielemans, "Theoretical comparison of motion correction techniques for PET image reconstruction", *Proc. IEEE Nuc. Sci. Symp. Med. Img. Conf.* pp. 1762-1767, 2006

[27] C. Tsoumpas, P. Aguiar, D. Ros, N. Dikaios and K. Thielemans, "Scatter simulation including double scatter" , *Proc. IEEE Nuc. Sci. Symp. Med. Img. Conf.*, pp. 1615-1619, 2005

[28] A.S. Goggin, J.M. Ollinger, "A model for multiple scatters in fully 3D PET", *Proc. IEEE Nuc. Sci. Symp. Med. Img. Conf.*, pp. 1609-1613, 1994

[29] M. Iatrou, R.M. Manjeshwar, S.D. Wollenweber, S.G. Ross and C.W.Stearns, "Out-of-field scatter estimation in 3D whole body PET", *Proc. IEEE Nuc. Sci. Symp. Med. Img. Conf.*, pp. 3886-3888, 2009.

[30] H. Qian, R. M. Manjeshwar, K. Thielemans, "A comparative study of multiple scatter estimations in 3D PET", *Proc. IEEE Nuc. Sci. Symp. Med. Img. Conf.*, pp.2700-2702, 2010

[31] K. Thielemans, R.M. Manjeshwar, X. Tao, E. Asma, "Lesion detectability in motion compensated image reconstruction of respiratory gated PET/CT", *Proc. IEEE Nuc. Sci. Symp. Med. Img. Conf.* pp. 3278-3282, San Diego, CA, 2006

[32] C. Liu, A. Alessio, L. Pierce, K. Thielemans, S. Wollenweber, A. Ganin, P.E. Kinahan, "Quiescent period respiratory gating for PET/CT", *Med. Phys.* 37(9):5037-5043, 2009

[33] Y. E. Erdi, S.A. Nehmeh, T. Pan, A. Pevsner, K.E. Rosenzweig, G. Mageras, E.D. Yorke, H. Schoder, W. Hsiao, O.D. Squire, P. Vernon, J.B. Ashman, H. Mostafavi, S.M. Larson, J.L. Humm, "The CT motion quantitation of lung lesions and its impact on PET-measured SUVs", *Jour. Nuc. Med.*, (45)8:1287-1292, 2004

[34] S. Nehmeh, Y. Erdi, C.C. Ling, K.E. Rosenzweig, H. Schoder, S.M. Larson, H. A. Macapinlac, O.D. Squire, J. L. Humm, "Effect of respiratory gating on quantifying PET images of lung cancer", *Jour. Nuc. Med.*, 43(7):876-881, 2002

[35] L. Boucher, S. Rodrigue, R. Lecomte, F. Benard, "Respiratory gating for 3-Dimensional PET of the thorax: Feasibility and initial results", *Jour. Nuc. Med.*, 45(2):214-219, 2004

[36] B.C. Vemuri, J. Ye, Y. Chen, C.M. Leonard, "Image registration via level-set motion: Applications to atlas-based segmentation" *Med. Imag. Anal.* 7(1):1-20, 2003

[37] S.D. Wollenweber, G. Gopalakrishnan, K. Thielemans, R.M. Manjeshwar, "Evaluation of the accuracy and robustness of a motion correction algorithm for PET using a novel phantom approach", *IEEE Trans. Nuc. Sci.*, 59(1):123-130, 2012

[38] S.Y. Chun and J.A. Fessler, "Noise properties of motion-compensated tomographic image reconstruction methods", *IEEE Trans. Med. Imag.*, in press, 2012

[39] S. Geman, D.E. McClure, "Statistical methods for tomographic image reconstruction", *Bull. Int. Stat. Inst.*, 52(4);5-21, 1987

[40] J. Qi, R.M. Leahy, "Iterative reconstruction techniques in emission computed tomography", *Phys. Med. Bio.*, 51(15):R541-R578, 2006

[41] E.U. Mumcuoglu, R. Leahy, S. R. Cherry, "Bayesian reconstruction of PET images: methodology and performance analysis", *Phys. Med. Bio.* 1:1777-1807, 1996

[42] J.W. Stayman and J.A. Fessler, "Regularization for uniform spatial resolution properties in penalized-likelihood image reconstruction", *IEEE Trans. Med. Imag.*, 19(6): 601-615, 2000

[43] J. Nuyts, D. Beque, P. Dupont, L.Mortelmans, "A concave prior penalizing relative differences for maximum-a-posteriori reconstruction in emission tomography", *IEEE Trans. Nuc. Sci.* 49(1):56-60, 2002

[44] J. Nuyts, C. Michel, L. Brepoels, L. DeCeuninck, C. Deroose, K. Goffin, F.M. Mottaghy, S. Stroobants, J. Van Riet, R. Verscuren, "Performance of MAP reconstruction for hot lesion detection in whole body PET/CT: an evaluation with human and numerical observers", *IEEE Trans. Med. Imag.*, 28(1):67-73, 2009

[45] J. Qi, R.M. Leahy,"A theoretical study of the contrast recovery and variance of MAP reconstructions from PET data", *IEEE Trans. Med. Imag.*, 18(4):293–305, 1999

[46] J.A.Fessler, "Spatial resolution properties of penalized-likelihood image reconstruction: Space invariant tomographs" *IEEE Trans. Img. Proc.*, 5(9):1346–58, 1996

[47] J. Colsher, J. Hsieh, J.B. Thibault, A. Lonn, T. Pan, S.J. Lokittz, T.G. Turkington, "Ultra low dose CT for attenuation correction in PET/CT" *Proc. IEEE Nuc. Sci. Symp. Med. Img. Conf.* pp. 5506-5511, Dresden, Germany, 2008

[48] T. Xia, A.M. Alessio, B. DeMan, R. Manjeshwar, E. Asma, P.E. Kinahan, "Ultra-low dose CT attenuation correction for PET/CT", *Phys. Med. Bio*, 57(2):309-328, 2012